JGR Oceans

RESEARCH ARTICLE
10.1029/2019JC015157

Mooring and Seafloor Pressure End Point Measurements at the Southern Entrance of the Solomon Sea: Subseasonal to Interannual Flow Variability

Arachaporn Anutaliya[1], Uwe Send[1], Janet Sprintall[1], Julie L. McClean[1], Matthias Lankhorst[1], and Jannes Koelling[1]

[1]Scripps Institution of Oceanography, La Jolla, CA, USA

Key Points:
- The observations reveal energetic subseasonal flow (37% of total variance) into the Solomon Sea associated with local and remote winds
- Rossby waves propagating from the central Pacific Ocean are well correlated with the inflow variability at seasonal and longer timescales
- The inflow strengthens and the seasonal cycle is suppressed during the 2015/2016 El Niño

Correspondence to:
A. Anutaliya,
aanutali@ucsd.edu

Citation:
Anutaliya, A., Send, U., Sprintall, J., McClean, J. L., Lankhorst, M., & Koelling, J. (2019). Mooring and seafloor pressure end point measurements at the southern entrance of the Solomon Sea: Subseasonal to interannual flow variability. *Journal of Geophysical Research: Oceans*, *124*, 5085–5104. https://doi.org/10.1029/2019JC015157

Received 19 MAR 2019
Accepted 2 JUL 2019
Accepted article online 6 JUL 2019
Published online 22 JUL 2019

Abstract Variability of the flow across the Solomon Sea's southern entrance was examined using end point subsurface moorings and seafloor pressure sensors, reconstructed velocity profiles based on satellite-derived surface velocity and bottom pressure-derived subsurface velocity, and 1993–2017 proxy volume transport based on satellite altimetry. The reconstructed velocity correctly represents the fluctuating surface flow and subsurface core providing a high-frequency continuous observing system for this sea. The mean equatorward volume transport over 0- to 500-m depth layer is 15.2 Sv (1 Sv $\equiv 10^6$ m^3/s) during July 2012 to May 2017. The measurements resolve the full spectrum of the volume transport including energetic subseasonal variability that fluctuates by as much as 25 Sv over one week. At low-frequency timescales, the study finds that linear Rossby waves forced by Ekman pumping in the interior of the Pacific influence not only seasonal fluctuations as found by previous studies but also interannual variability. As found previously, the El Niño–Southern Oscillation highly influences interannual volume transport. During the 2015/2016 El Niño, observations show the seasonal cycle to be suppressed from the second half of 2014, prior to the mature phase of the El Niño, to September 2016 along with an increase in across-transect transport. At subseasonal timescales, local Ekman pumping and remote wind stress curl are responsible for a third of the subseasonal variance. The study highlights the importance of high-frequency observations at the southern entrance of the Solomon Sea and the ability of a linear Rossby model to represent the low-frequency variability of the transport.

Plain Language Summary The Solomon Sea, located in the tropical southwest Pacific Ocean, is characterized by energetic currents that transport water from the subtropical South Pacific to the equatorial Pacific. In this study, we quantify the amount of water being transported through the Solomon Sea to understand how and why it changes over time. Over the observing period (July 2012 to May 2017), a mean water volume of 15.2 Sv (1 Sv $\equiv 10^6$ m^3/s) flows into the Solomon Sea at its southern entrance. The flow can change greatly over short time period ($\pm$25 Sv over 1 week) as being modified by winds over the Solomon Sea and further upstream over the Coral Sea. The observed inflow also has distinct interannual variability and a seasonal cycle with a minimum in March/April and a maximum in July/August. On these timescales, the flow fluctuates up to $\pm$10 Sv as being influenced by the winds over the equatorial and tropical Pacific Ocean. During the 2015/2016 El Niño, our observations show that the equatorward flow via the Solomon Sea strengthens but the seasonal cycle is suppressed. We also showed that the flow can be efficiently monitored using only a pair bottom-pressure sensors and satellite altimetry.

1. Introduction

The surface New Guinea Coastal Current (NGCC) and the subsurface New Guinea Coastal Undercurrent (NGCU) serve as the Low Latitude Western Boundary Current (LLWBC) of the subtropical cell in the Pacific Ocean (McCreary & Lu, 1994). This LLWBC system is a major conduit of flow between the South Pacific Ocean and the equatorial Pacific as it replenishes the equatorial Warm Pool and supplies the Equatorial Undercurrent (EUC; Tsuchiya et al., 1989; Grenier et al., 2011) and the Indonesian Throughflow (Fine et al., 1994; Waworuntu et al., 2000). Since the equatorial Pacific impacts large-scale atmospheric convection and climate modes (Gu & Philander, 1997; McPhaden & Zhang, 2002; Picaut et al., 1996), such as El Niño–Southern Oscillation (ENSO; Melet et al., 2010; Davis et al., 2012; Zilberman et al., 2013; Ganachaud et al., 2014), variability of the NGCC/NGCU current system potentially influences climate variability.

In the past, historical shipboard Acoustic Doppler Current Profiler data, Spray gliders, and Argo floats have been used to quantify the mean and variability of the NGCC/NGCU current system. The time series mean of the volume transport into the Solomon Sea (hereafter referred to as the inflow) at its southern entrance has been found to be 15 Sv over 0–300 m, 15 Sv over 0–700 m, and 19 Sv over the 0- to 1,000-m layer, respectively (Cravatte et al., 2011; Davis et al., 2012; Zilberman et al., 2013). Seasonal variations as high as 30 Sv are captured by glider measurements at the southern entrance (Davis et al., 2012); the volume transport reaches its minimum in February and maximum in July–August (Kessler et al., 2019). Interannual variability of the circulation in the Solomon Sea is strongly influenced by ENSO signals (Melet et al., 2013; Melet, Gourdeau, & Verron, 2010). Strengthening (weakening) of the equatorward flow through the Solomon Sea occurs during El Niño (La Niña) events (Davis et al., 2012; Zilberman et al., 2013). None of these measurement systems are able to resolve the variability on shorter timescales (i.e., the subseasonal variability that is <60 days).

In this study, we address the variability of the volume inflow at the southern entrance of the Solomon Sea at subseasonal, seasonal, and interannual timescales using high-frequency end point measurements from dynamic height moorings and seafloor pressure sensors (PIES: Pressure with Inverted Echo Sounders; Kennelly et al., 2007). The measurements are available hourly and resolve signals with periods as short as 3 days; hence, the time series are not subject to aliasing such as that which might result from less frequent sampling in the presence of high eddy activity in this region (Gourdeau et al., 2014; Hristova & Kessler, 2012; Melet, Gourdeau, & Verron, 2010). Moreover, these continuous observations allow for the development of a volume transport proxy using satellite altimeter data over the observational period, and thus allows extension of the time series to the 1993–2017 period. The 25-year proxy time series provides us with a valuable data set to examine the interannual variability of the Solomon Sea inflow.

To understand the governing mechanisms associated with the variability of the circulation in the Solomon Sea, numerical ocean model simulations have shown that the regional circulation is influenced by the annual march of the trade winds and the Asian monsoon winds (Hristova & Kessler, 2012; Kessler & Gourdeau, 2007). Further, the seasonality of the trade winds produces Rossby waves that affect the South Equatorial Current (SEC) approximately from 2° to 10°S (Chen & Qiu, 2004; Melet et al., 2010). The arrival of downwelling (upwelling) Rossby waves at the Solomon Strait excited by the annual winds from the Central Pacific in March–April (September–October) produces southeastward (northwestward) surface flow at the southern entrance of the Solomon Sea (Gourdeau et al., 2014; Melet, Gourdeau, & Verron, 2010). In the southwestern Pacific (from approximately 10°S to 30°S), wind stress curl dominates the annual variability of the thermocline depth (Chen & Qiu, 2004; Kessler & Gourdeau, 2007; Wang et al., 2000) and potentially influences the Solomon Sea inflow. Observations of sea surface height from satellite altimetry (Chen & Qiu, 2004; Melet, Gourdeau, & Verron, 2010), thermocline depth (Wang et al., 2000), and surface velocity from satellite-tracked drifters (Hristova & Kessler, 2012) demonstrate the influence of Rossby waves and wind stress curl in the western subtropical Pacific on the annual variability of the flow. However, to date, no high-frequency in situ measurements have been available to demonstrate the influence of local and remote forcing on the regional circulation, particularly at the subseasonal timescale. Therefore, using our observations, we also aim to examine the role of Rossby waves, the subtropical wind stress curl, and local winds on the variability of the Solomon Sea inflow at subseasonal, seasonal, and interannual timescales.

The paper is organized as follows. The data sets and methodology are described in section 2 and 3, respectively. Section 4 presents the estimated mean and variability at subseasonal, seasonal, and interannual timescales of the current system derived from the end point measurements. Section 5 describes the impact of Rossby waves and local and remote winds on the variability of the inflow into the Solomon Sea. Discussion of the results and a summary are found in sections 6 and 7, respectively.

2. Data sets

2.1. In Situ Measurements

A subsurface mooring and a PIES were deployed on either side of the southern Solomon Sea, spanning a section sufficiently far from the equator to compute geostrophic currents across the section. One site is near Gizo, Solomon Islands (8.2°S, 157.0°E), and the other near Misima island, Papua New Guinea (10.6°S, 152.8°E). Figure 1 shows a map of the study area, and Table 1 contains the deployment particulars.

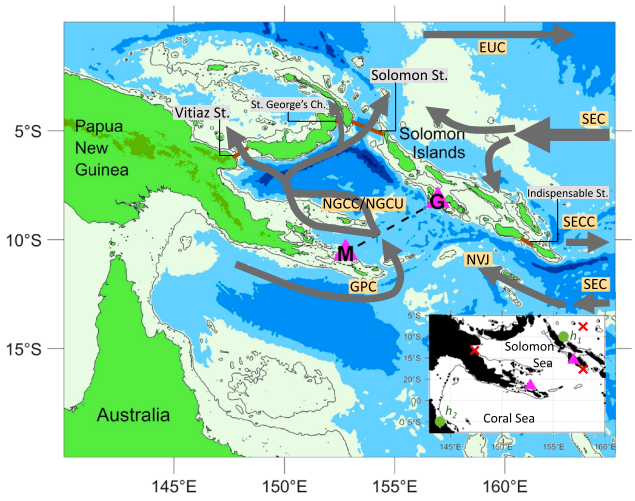

Figure 1. Bathymetry of the Solomon Sea and its surroundings along with the location of the moorings and PIES (magenta triangles) near Misima (M) and Gizo (G) Islands. Schematic of dominant Solomon Sea currents are represented by the gray arrows; NGCC is New Guinea Coastal Current, NGCU is New Guinea Coastal Undercurrent, GPC is Gulf of Papua Current, NVJ is North Vanuatu Jet, EUC is Equatorial Undercurrent, SEC is South Equatorial Current, SECC is South Equatorial Countercurrent. Black contours are plotted for 0- and 1,000-m depth. The inset shows locations used to construct the proxy volume transport (maroon crosses) and Δh (green circles).

The subsurface moorings collected data during multiple deployments from mid-2012 through mid-2017 and were discontinued afterward. Each mooring contained six instruments for temperature and salinity distributed over the upper 500 m of the water column (Table 1). The intent of these measurements is to provide vertical profiles of density, and thereby the vertical shear of the geostrophic flow by differencing dynamic height (or geopotential anomaly) profiles measured at the two measuring sites. The actual instrumental sensors are for temperature and conductivity, and a subset of the instruments had pressure sensors. Pressure values for the remaining instruments were determined by interpolation along the (known) mooring wire lengths. Before each deployment and after each recovery, a calibration/validation effort was carried out that compared mooring sensors either against ship-based CTD casts (following Kanzow et al., 2006) or against a reference instrument submerged locally at a pier. Salinity water samples from bottles were used as well. Sensor drift was removed assuming linear drifts over time. In the adjusted data, salinity accuracy is estimated conservatively at ~0.01–0.02, with the largest errors in the upper instruments due to biofouling of the conductivity sensor.

PIES were deployed on the seafloor at approximately 300-m depth, which is the depth of the subsurface velocity core at the Solomon Sea southern entrance (Davis et al., 2012). The PIES were deployed in early 2012 at both sites, and after multiple redeployments, the measurements are still continuing to date (March 2019). Table 1 lists the deployment details. PIES measure seafloor pressure and water column acoustic travel time. Here, only the pressure data are used, which are particularly accurate from this instrument. The acoustic travel time data are available in principle, but their usefulness is limited by the shallow instrument deployment depth and they are redundant with the much more accurate water column information from the temperature and salinity data used here. The data processing procedure for the removal of the mean value, trend, and tides in the pressure signal follows that described by Kennelly et al. (2007). Ultimately, the data product is a time series of pressure anomalies, from which geostrophic velocity fluctuations at the depth of the PIES can be calculated. This is akin to a geostrophic reference "level of known motion." However, because the mean and low-frequency variability are removed as a consequence of data processing (section 3.2), only velocity fluctuations on timescales faster than each individual deployment duration (2–4 years) are captured in these data.

Spray gliders have been operated in the Solomon Sea since mid-2007; they measure temperature, salinity, and depth-averaged current across the southern entrance of the Solomon Sea in the upper 1,000 m of the

Table 1
Deployment Times, Locations, and Instrument Depths of the Moorings and PIES at Misima and Gizo

Deployment	Time	Location Misima	Instrument depth (m)	Time	Location Gizo	Instrument Depth (m)
Mooring 1	07/2012 to 08/2015	10°34.51′S, 152°41.53′E	64*, 112, 162, 261*, 361, 507*	07/2012 to 03/2015	08°14.04′S, 156°56.34′E	60*, 109, 158, 257*, 357, 504*
Mooring 2	08/2015 to 05/2017	10°34.52′S, 152°41.40′E	62*, 112, 162*, 262, 362*, 508*	03/2015 to 07/2016	08°14.12′S, 156°56.30′E	63*, 110, 159, 258*, 359, 508*
Mooring 3	-	-	-	07/2016 to 11/2017	08°14.21′S, 156°56.28′E	89*, 138, 188, 287*, 386*, 534*
PIES 1	02/2012 to 09/2014	10°36.12′S, 152°47.10′E	311	02/2012 to 07/2016	08°12.90′S, 156°57.45′E	320
PIES 2	02/2012 to 09/2014	10°36.12′S, 152°47.10′E	311	02/2012 to 07/2016	08°12.90′S, 156°57.45′E	320
PIES 2	09/2014 to 09/2018	10°36.11′S, 152°47.15′E	285	07/2016 to ongoing	08°12.89′S, 156°57.42′E	326
PIES 3	09/2018 to ongoing	10°36.13′S, 152°47.14′E	285	—	—	—

Note. The six instruments of every mooring deployment each had sensors for conductivity and temperature, and at least three of each mooring (marked with asterisks) also had pressure. Pressure with Inverted Echo Sounders (PIES) instruments have sensors for seafloor pressure and water column acoustic travel time.

water column (Davis et al., 2012; Kessler et al., 2019). The gliders typically take about 1 month to cross the southern entrance, making 100–150 profiles during each transect crossing. They crossed the entrance every month prior to 2013 and roughly every 3 weeks afterward. The glider measurements were used to correct the satellite-derived surface velocity. Also, the measurements provide an independent estimate of the volume transport at the Solomon Sea southern entrance.

Temperature and salinity profiles from Argo floats were utilized to extrapolate the density profiles between the surface and the shallowest mooring measurement (typically 60–90 m; Table 1). There were 68 and 123 Argo floats within 1° of the mooring at Gizo and Misima, respectively. Vertical resolution of the temperature, salinity, and pressure sampled by the Argo floats was 10 m near the surface and 50 at 500 m. Argo floats were also used to determine an error associated with the mooring-derived sheared flow due to vertical density interpolation.

2.2. Remotely Sensed Data

The all-sat-merged absolute dynamic topography (ADT) gridded products, deduced from the mean dynamic topography and the gridded satellite sea level anomaly (SLA), are available on a 0.25° grid at daily resolution and cover the period of 1993–2017. The data were linearly interpolated in space to the Gizo and Misima sites. The ADT products at the two observing sites were used to calculate the surface geostrophic velocity, and the SLA products were used to construct a proxy for the volume transport.

Surface wind data were used to better understand the impact of local Ekman pumping and remote winds on the inflow variability and also to examine the impact of Ekman transport on the across-transect volume transport. The Version 2 Cross-Calibrated Multi-Platform (CCMP) from Remote Sensing Systems provided gridded surface vector winds on a 0.25° grid with a temporal resolution of 6 hours (Wentz et al., 2015). The CCMP winds were available from July 1987 to December 2017.

3. Methodology

3.1. Sheared Velocity

Density was calculated from the measured temperature and salinity at six depths over the water column (Table 1), then interpolated onto a 1-m vertical grid. Cubic interpolation was performed below the depth of the shallowest mooring sensor, while the missing surface portion was derived from the mean density profile measured by nearby Argo floats. Mean sheared velocity across the transect between the mooring sites (v_{sheared}) was calculated from the difference of the dynamic height profiles measured between Misima (M) and Gizo (G), similar to the method described by Kanzow et al. (2006):

$$v_{\text{sheared}}(p,t)=\frac{1}{f\Delta x}\int_{p_{\text{ref}}}^{p}\left(\delta(p,t)^{G}-\delta(p,t)^{M}\right)\mathrm{d}p, \tag{1}$$

where f is the Coriolis parameter at the mean latitude (9.4°S), Δx is distance between the two measurement sites (~532 km), p_{ref} is pressure at the reference level of 500 dbar, and δ is specific volume anomaly defined as

$$\delta(p,t)=\frac{1}{\rho(p,t)}-\frac{1}{\rho_{(35,0)}}(p)\ , \tag{2}$$

$\rho_{(35,0)}$ is density of seawater with salinity of 35 and temperature of 0 ° C. To estimate the uncertainty associated with interpolating density profiles from the mooring measurements, "mooring-like" density profiles were estimated from subsampling 68 and 123 Argo density profiles measured near Gizo and Misima at the mean depth of the six mooring sensors (Table 1). The Argo float density profiles were treated as the true density profiles and subsampled like a mooring to obtain an uncertainty of 2.7 Sv in the sheared volume transport. The estimated uncertainty is associated with density interpolation between mooring sensors and extrapolation of the density profiles toward the surface. The surface geostrophic velocity relative to 500 m derived from the mooring density profiles, glider data, and Argo float data have a similar mean value; the root-mean-square (rms) difference is smaller than 4.5 cm/s. Vertically integrated sheared flow across the transect calculated from the three data sets also agrees well; the mean values agree within 2 Sv. This suggests that the uncertainty associated with mooring density interpolation and extrapolation in the sheared

transport estimate is small. With the instrumental errors, the total rms uncertainty in the sheared transport across the transect is estimated to be 3.1 Sv.

3.2. Velocity Fluctuation at PIES Depth

Velocity fluctuations at the mean depth of the PIES during each deployment (~300 m) were calculated from the PIES bottom pressure measurements and were combined with v_{sheared} in order to obtain the total geostrophic volume transport variability. The PIES bottom pressure measurements were averaged over 1-hr bins. Then the seven most dominant tidal constituents were removed using UTide (Codiga, 2011). In addition, an exponential-linear trend associated with pressure drift (Kennelly et al., 2007) was removed. At these measurement sites, the dynamic range of the pressure fluctuation is 0.2 dbar and the sensor drift over a 4-year deployment ranges from less than 0.1 to 0.6 dbar. To remove tidal signals that might remain in the detrended records, the tidal constituents that were previously removed were added back to the detrended pressure fluctuation, after which the seven major tidal constituents were again removed. Finally, a 3-day low-pass Butterworth filter (the inertial period at this latitude) was applied to the pressure fluctuations. Velocity fluctuations at the depth of the PIES (v'_{sub}) were estimated from the pressure fluctuations (p'_{sub}; Kanzow et al., 2006):

$$v'_{\text{sub}}(t)=\frac{1}{f\Delta x}\left(\frac{p'^{G}_{\text{sub}}(t)}{\rho^{G}}-\frac{p'^{M}_{\text{sub}}(t)}{\rho^{M}}\right) \tag{3}$$

The barotropic volume transport fluctuations are then calculated assuming a slab flow which is a product of v'_{sub}, Δx and the 500-m layer. The rms error associated with the slab flow including uncertainty from the detrending and instrument error is 4.8 Sv.

3.3. Absolute Geostrophic Velocity

To produce the absolute geostrophic velocity, v_{sheared} is referenced to the depth of the PIES at ~300 m. Then, the same fluctuation for the entire water column (v'_{sub}) is added to the sheared profiles. However, the resulting transport still needs a constant offset to adjust for the unknown vertical placement of each PIES with respect to the geoid. The offset is found from an alternative estimate of the volume transport, calculated from the mooring measurements and ADT where the ADT provides an estimate of the surface absolute geostrophic velocity, and the moorings provide sheared velocity profiles relative to the surface. The mean component in the ADT, however, is subject to 5–10 cm of error over the Solomon Sea (Rio & Hernandez, 2004); thus, a time-invariant correction to the ADT-derived velocity is needed. The correction is estimated as the difference between surface velocity derived from the ADT and that from gliders, which is 3.3 cm/s over the period when glider data are available (2007–2016). Thus, 3.3 cm/s was subtracted from the ADT-derived surface absolute geostrophic velocity (hereafter referred to as ADT_c) before it is combined with the mooring sheared velocity profiles that are referenced to the surface. The offset velocity between the mooring/PIES and mooring/ADT_c velocity profiles, determined separately over each PIES deployment period, is given by the difference between the mean profile of the two estimates.

The resulting absolute geostrophic velocity derived from our in situ measurements resolves frequencies lower than the inertial period in this region (3 day) and spans a period of nearly 5 years (July 2012 to May 2017) overlapping with the 2015/2016 El Niño event. Thus, the resulting time series are useful to understand inflow variability on timescales longer than 3 days, that is, subseasonal, seasonal, and interannual timescales.

3.4. Proxy Volume Transport From the Satellite SLA

In addition to the observations, a proxy for the volume transport derived from the satellite SLA is used to examine variabilities on seasonal and interannual timescales. The proxy time series is based on a linear regression between the observed absolute volume transport in the 0- to 500-m layer over the 5-year observing period and satellite SLA at three locations: near Gizo Island (157.9°E, 9.1°S), near Vitiaz St. (147.4°E, 7.4°S), and within the SEC (157.9°E, 5.1°S; Figure 1). The locations were selected empirically to maximize the correlation between the proxy volume transport and the observations, but they also represent regions responsible for the flow variability in the Solomon Sea (Cravatte et al., 2011; Hristova & Kessler, 2012; Melet, Gourdeau, & Verron, 2010). As the satellite-derived SLA near Vitiaz St. used in the regression is located in the coastal region where large uncertainties can arise in satellite SLA, it is compared to the nearby tide gauge station at Lae (Holgate et al., 2013; PSMSL, 2019), Papua New Guinea, (147.0°E, 6.75°S). The

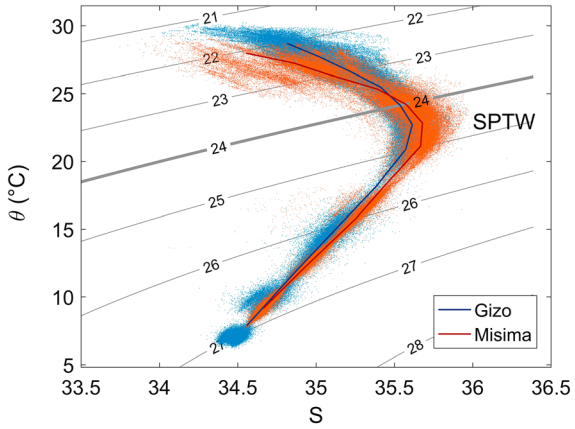

Figure 2. Scatterplot between potential temperature (θ) and salinity (S) at Gizo (blue) and Misima (orange) measured by moorings between July 2012 and May 2017 at six depth levels in the top 500 m of the water column overlaying isopycnal (σ_θ) contours. Mean θ-S at Gizo and Misima is plotted in dark blue and brown lines, respectively.

available tide gauge record is between September 1984 and January 2000 with intermittent gaps that are as large as 13 months. For the overlapping period of ~63 months, the satellite SLA agrees reasonably well with tide gauge data ($r = 0.75$). Since the satellite SLA has roughly weekly resolution, a 10-day low-pass filter was applied to the volume transport and SLA time series. The concurrent SLA proxy time series can then be extended using the full 25-year satellite SLA measurement from 1993 to 2017. During the period overlapping with the observations, the proxy volume transport captures 64% of the variance in the observed transport. The explained variance is significantly higher than a proxy based simply on SLA at the two mooring sites, which captures 50% of total variance of the observed inflow, while using more than three locations did not substantially improve the skill. In addition, as pointed out by Kessler et al. (2019), a proxy derived simply from SLA at two locations across the southern entrance can easily fail to capture volume transport variations when the dominant subsurface layer flow does not correlate with flow in the surface layer.

For simplicity, the total volume transport across the southern entrance of the Solomon Sea over the 0- to 500-m depth layer will be referred to as the NGCC/NGCU current system, even though the NGCC and NGCU are usually confined to the western part of the basin and the NGCU often extends to 1,000 m (Davis et al., 2012; Gasparin et al., 2012; Germineaud et al., 2016). We are decomposing the volume transport into the surface layer flow, defined as flow across the southern entrance of the Solomon Sea from the surface to $\sigma_\theta = 24.0$ (equivalent to the mean depth of 130 m), and the thermocline layer flow, defined as the flow from $\sigma_\theta = 24.0$ to 500 m. However, since our end point observing system cannot capture the actual depth of the $\sigma_\theta = 24.0$ isopycnal along the transect, the surface layer transport was estimated as the vertical integral of the across-transect mean velocity profile between the surface to the horizontal-average (but time-variable) depth of the $\sigma_\theta = 24.0$ isopycnal between the two moorings multiplied by the transect length. The thermocline transport was computed similarly, except the vertical integral was calculated between the time-varying average depth of the 24.0 isopycnal and 500 m. The rms errors associated with the use of the across-transect average isopycnal depth and across-transect mean velocity profile rather than the true (but unknown) varying isopycnal depth and velocity along the transect are 0.8 and 1.3 Sv in the surface and thermocline layer, respectively. In each layer, the error was estimated using output from a global coupled 0.1° Parallel Ocean Program2/Los Alamos Sea Ice Model (POP2/CICE4; Appendix A) simulation as the rms difference between an end point mooring-like volume transport and that calculated from the model density and velocity fields. The flow in the surface and thermocline layers will be interchangeably referred to as the NGCC and NGCU, respectively. Inflow variability in three different frequency bands will be considered: between 3 and 60 days (subseasonal variability), between 60 and 400 days, and lower than 400 days (interannual variability). Separately, the seasonal cycle is examined.

4. Mean and Variability of the NGCC and NGCU

4.1. Temperature and Salinity Relationship

Potential temperature versus salinity relationships from the 2012 to 2017 mooring deployments at the Misima (western side) and Gizo (eastern side) sites shows a lower salinity range in the water column at Gizo relative to that at Misima (Figure 2), similar to the salinity profiles measured by gliders (Gourdeau et al., 2017). The signature of the South Pacific Tropical Water (SPTW), identified by a salinity maximum at $\sigma_\theta = 24.5$, is apparent at both locations. In the thermocline layer, the Misima salinity is up to 0.1 higher than that at Gizo as the Gulf of Papua Current (GPC) and the NVJ that transport SPTW into the Solomon Sea mainly flow along the western part of the basin. In addition, the Gizo mooring salinity measurements show a distinct seasonal cycle at the depth of the salinity maximum ($\sigma_\theta = 24.5$); relatively low salinity is present in March–April and high salinity is present in July–August. The seasonality in salinity at Gizo yields higher variability in dynamic height compared to that at Misima. Therefore, seasonal variability in the sheared

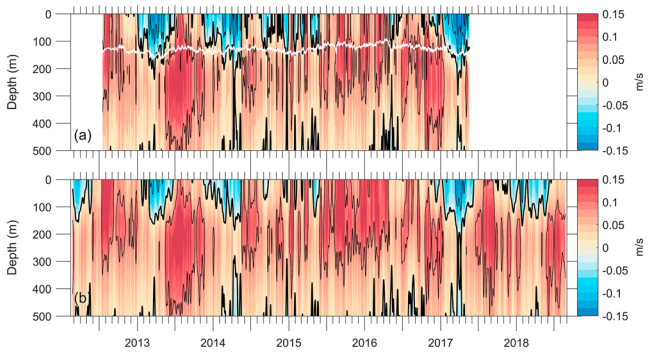

Figure 3. Three-day low-pass filtered across-transect mean velocity time series estimated from (a) moorings and Pressure with Inverted Echo Sounders (PIES), and (b) PIES, ADT_c, and the first two empirical orthogonal functions (EOFs) derived from (a). The black thick line highlights the zero contour, the black thin lines represent 0.1 m/s contours, and the white line in (a) shows $\sigma_\theta = 24.0$.

component of the cross-passage volume transport is largely contributed by dynamic height variability in the eastern Solomon Sea at Gizo. The sheared transport produced by the Gizo dynamic height and the *mean* profile of Misima dynamic height can capture 83% of the sheared transport variance.

4.2. Mean and Overview of the Inflow Variability

4.2.1. Vertical Structure

Horizontally averaged geostrophic velocity across the transect is presented in Figure 3a. The surface velocity is highly fluctuating. A poleward-flowing current is distinct from around January to May in 2013, 2014, and 2017. The poleward current in 2015 is weak, and in 2016, it is nearly absent. Between 120 and 300 m, a subsurface velocity maximum that intensifies in June–September of 2013 is present. To further investigate the vertical structure of the volume transport through the Solomon Sea, the time series of the velocity fluctuation profiles derived by removing the time-mean velocity profile over the period of the observations (Figure 3a) are decomposed into empirical orthogonal functions (EOFs) and the corresponding principal components (PCs). The first two modes explain 98% of the variance (Figure 4). The first leading EOF mode, explaining 82% of the velocity variance, is surface-intensified and decays with depth. The corresponding PC highly correlates with volume transport in the 0- to 500-m depth layer ($r = 0.97$). The second EOF mode has a sheared structure with one maximum at the surface and the other at 300 m emphasizing the subsurface fluctuation in the transport. The depth of reversal is at 140 m similar to the mean depth of $\sigma_\theta = 24.0$ supporting the choice of using $\sigma_\theta = 24.0$ to separate the NGCC from the NGCU. The second PC corresponds more closely to the absolute geostrophic velocity at 500-m depth ($r = 0.74$).

4.2.2. Mean and Variability

The absolute geostrophic transport in the upper 500 m estimated from the moorings and PIES over the period of July 2012 to May 2017 fluctuates between −20.6 and 43.9 Sv (positive equatorward) with a mean of 15.2 Sv, in good agreement with estimates from previous observations (Cravatte et al., 2011; Davis et al., 2012; Zilberman et al., 2013) and numerical simulation (Djath et al., 2014). The temporal standard deviation is 11.0 Sv (Figure 5a and Table 2). The rms error associated with the volume transport calculation, which includes that from mooring interpolation and extrapolation (2.7 Sv), detrending of the PIES time series (3.0 Sv), instrument error (4.4 Sv), unresolved across-transect eddy propagation (3.0 Sv), and the use of constant f (1.5 Sv), is 6.8 Sv (variances of the different error components were added together; Thomson & Emery, 2014). In the surface layer, the volume transport across the transect ranges from −15.6 to 13.0 Sv with a mean of 1.7 Sv and has a strong annual cycle in the first 2 years of the record (July 2012–2014). In the

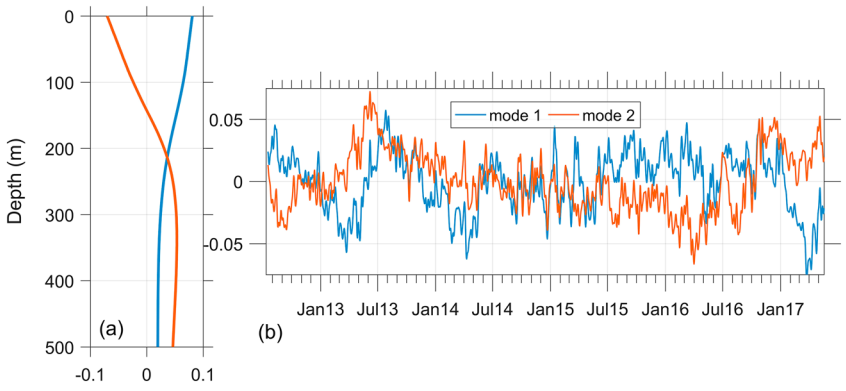

Figure 4. (a) The first two empirical orthogonal functions and (b) their corresponding principal components computed from the 3-day low-pass filtered mooring/Pressure with Inverted Echo Sounders velocity time series (Figure 3a).

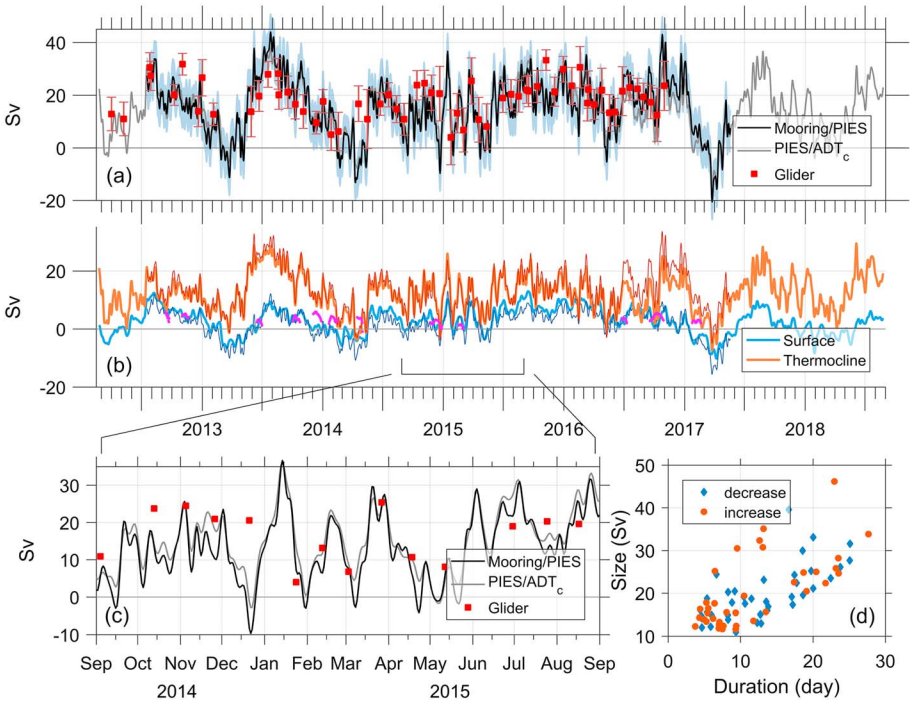

Figure 5. (a) Three-day low-pass filtered absolute geostrophic volume transport calculated from the Pressure with Inverted Echo Sounders (PIES)/ADT$_c$ (gray), mooring/PIES observations (black) with the associated uncertainty shown in blue shading and volume transport calculated from glider measurements (red squares) with the estimated uncertainty shown in red bars; (b) the volume transport in the surface (thin blue) and thermocline (thin orange) layer computed from mooring/PIES measurements compared to those from PIES/ADT$_c$ reconstruction (thick lines). The magenta thick lines show some examples of net across-transect volume transport produced by an eddy propagating through the transect assuming a constant *f*. (c) Magnification of (a) over September 2014 to August 2015, and (d) scatterplot showing the magnitude and duration of extreme events identified from the 3-day low-pass filtered volume transport estimated from the mooring/PIES measurements.

thermocline layer, the volume transport is usually equatorward and ranges from −5.0 to 33.6 Sv with a mean of 13.5 Sv (Figure 5b and Table 2).

The mean of the proxy transport is in good agreement with the shorter observed period at 12.4 Sv with a standard deviation of 9.3 Sv (Table 2). Note that the mean volume transport of the proxy and the observations is the same (15.2 Sv) during the overlapping period by construction as the proxy volume transport is derived from a linear regression between the observed volume transport and SLA over that period. However, when the regression-derived coefficients are applied to the SLA outside of that period, it can result in a different time mean over the extended period (1993–2017).

The glider transport error bar (Figure 5a) is estimated as the standard deviation of the mooring/PIES time series spanning 6 weeks centered at the time when the glider reaches its midcrossing location. The error bar reflects the error from asynchronous sampling across the southern entrance by the glider. The mooring/PIES transport agrees well within their errors with most of glider transport estimates; the rms difference is 7.1 Sv. During May–November 2013, volume transport calculated from the mooring/PIES measurements is consistently higher than that from the glider measurements (Figure 5). Therefore, we compared the SLA derived from the mooring and PIES at the Gizo site, which has the dominant dynamic height signal, to the satellite along-track SLA during that period (not shown) to verify the mooring/PIES measurement. The along-track satellite SLA increases from April to July of 2013 and matches the amplitude of the mooring/PIES SLA. This evidence strongly corroborates the transport result calculated from the mooring and PIES measurements during this period. Ekman transport across the transect, which is not captured by our geostrophic transport estimates, is relatively small as the prevailing wind over the Solomon Sea is along the basin (northwestward or southeastward wind); the across-transect Ekman transport is at most 2.0 Sv with an rms value of 0.5 Sv.

Table 2
Mean and Standard Deviation of Volume Transport at the Southern Entrance of the Solomon Sea in the Upper 500 m of the Water Column Estimated From Different Techniques

Data set	Time period	Mean (Sv) (surface/thermocline)	Standard deviation (Sv)
Mooring/PIES	July 2012 to May 2017	15.2 (1.7/13.5)	11.0
PIES/ADT_c	February 2012 to September 2018	15.0 (2.7/12.3)	9.4
Proxy from ADT_c	January 1993 to December 2017	12.4	9.3

Note. Mean volume transport in the surface and thermocline layers is shown in the parenthesis. PIES = Pressure with Inverted Echo Sounders; ADT = absolute dynamic topography.

4.2.3. Using the Vertical EOF Modes to Reconstruct Volume Transport From PIES Measurements and the ADT_c

In addition to the mooring/PIES observations, the volume transport inflow can be estimated from subsurface velocity derived from the PIES measurements, surface velocity derived from the ADT_c, and the first two vertical EOF modes from the 3-day low-pass mooring/PIES time series (Figure 4a). The sole use of PIES and ADT_c allows for a more cost-effective means of long-term monitoring of the NGCC/NGCU at the southern Solomon Sea. Compared to the proxy volume transport that only uses the ADT_c, the addition of the PIES subsurface measurements both provides information on the vertical structure of the transport (Figure 3b) as well as improves the correlation of the volume transport with that computed from mooring/PIES measurements ($r = 0.95$; Figure 5a). A profile of horizontally averaged velocity across the transect is reconstructed as a linear combination of the first two EOF modes constrained by two direct measurements of geostrophic velocity derived from the ADT_c and PIES. The reconstructed velocity time series not only show the surface fluctuation but also the subsurface core of the current (Figure 3b). The time series resolves variability on various timescales (Figures 5a and b) including much of the highly fluctuating subseasonal variability that cannot be resolved by the ADT_c alone (Figure 5c). The PIES/ADT_c combination also provides 6.5 years of inflow estimates from March 2012 to September 2018 and thus is useful for examining the inflow condition during and after the 2015/2016 El Niño.

The surface and thermocline volume transport was estimated as the reconstructed flow above and below the time-mean $\sigma_\theta = 24.0$ isopycnal depth of 130 m (Figure 5b), assuming a constant depth layer yields uncertainty of 0.7 Sv in both the surface and thermocline layers. In the upper 500 m of the water column, the rms difference between the reconstructed and observed volume transport is 3.2 Sv over the overlapping period (Figure 5a). The largest discrepancy is near the surface (Figures 3 and 5b) reflecting the inconsistency between the surface geostrophic velocity derived from the ADT_c and that estimated from the surface extrapolation of mooring dynamic heights.

Although the reconstructed velocity profile depends on the first two vertical EOF modes, it is not sensitive to the detailed structure of the EOFs. Using EOF modes calculated from glider measurements with one surface-intensified mode and one sheared mode with a subsurface maximum at approximately 300 m, the resultant velocity profiles are not significantly different from that reconstructed with EOFs from moorings and the PIES.

4.3. Variability of the Solomon Sea inflow

4.3.1. Subseasonal Variability

The volume transport over the 0- to 500-m depth layer with frequencies lower than the inertial period (3 days) derived from mooring and PIES measurements reveals sudden changes in the inflow at the southern entrance of the Solomon Sea that are as large as 25 Sv over 1 week (Figure 5c). Extreme transport events are defined here as sudden changes in volume transport that are larger than the standard deviation of the volume transport (10.4 Sv; Table 2) that occur over less than 30 days with a rate greater than 1 Sv/day. The extreme events are scattered throughout the record but are more extreme and abundant during the onset of the 2015/2016 El Niño (from the end of 2014 to August 2015). A scatterplot shows the distribution of the event sizes (Figure 5d). The rate of change in volume transport ranges from 1 Sv/day (by construction) to 3.9 Sv/day. Variance of the volume transport in the subseasonal frequency band (3–60 days) accounts for 37% of the total variance.

Remotely sensed observational and numerical studies have suggested that mesoscale eddies are abundant at the entrance of the Solomon Sea (Hristova et al., 2014; Melet, Gourdeau, & Verron, 2010). We want to explore whether these sudden changes we observe in the transport might be related to eddy variability at the entrance to the Solomon Sea. The mesoscale eddies in the Solomon Sea are more numerous in March–May and during La Niña conditions, while fewer eddies are observed in July–August and during El Niño conditions (Gourdeau et al., 2014; Hristova et al., 2014; Qiu & Chen, 2004). When an eddy propagates across our observing transect, calculation error can arise as the eddy is not fully sampled by our end point measurements. The across-transect volume transport is calculated based on the difference between dynamic height measured by the two end point moorings assuming a constant f of the midlatitude, although the moorings are at different latitudes (Figure 1). In a scenario of a symmetric eddy propagating across the observing transect, dynamic height at each flank of the eddy would adjust to compensate for the difference in f along the transect to balance the volume transported by the two flanks. This results in a net gradient in dynamic height which is observed by the moorings. With the constant f assumption, our calculation then yields a volume transport, although the eddy does not transport volume.

To estimate the error in our transport calculation arising from the cross-transect eddy propagation, 12 eddies were manually identified from the satellite SLA over the observing period. For the identified eddies, we calculated volume transport from the SLA using a constant f and 500-m depth layer to simulate that calculated from the mooring measurements. This estimate is compared to the "more resolved" volume transport calculated by varying f along the transect (Appendix B). The difference between the two estimates (V_e) roughly reflects an error of volume transport that our calculation produces when an eddy is present at the transect: examples are indicated in Figure 5b. This exercise illuminates two important results. First, the subseasonal fluctuations due to the calculation error associated with the eddies rarely coincide with the observed extreme transport events. Second, the magnitude of the transport error attributed to the presence of an eddy is much smaller than the extreme transport events. The magnitude of V_e is at most 6.0 Sv when assuming an eddy depth of 500 m (Figure 5b) and only ~3.6 Sv when an eddy depth of 300 m is assumed. Our observations show the abundance of the extreme transport events during the 2015/2016 El Niño (the end of 2014 to August 2015; Figure 5a) suggesting that the events are not related to the presence of mesoscale eddies. Also, the extreme transport events are often associated with sudden changes in both the surface and thermocline layers (Figure 5b), while the eddies are thought to intensify roughly over the upper 150 m (Gourdeau et al., 2017; Hristova et al., 2014).

In addition, Kessler et al. (2019) found that the dominant subseasonal variability at the surface is associated with the basin-scale eddy that propagates along the major axis of the Solomon Sea from the southern entrance toward the equator with a speed of ~0.20 m/s. The analysis suggests a possibility of subseasonal variability in the transport observed by the moorings as an artifact of their locations that are not on the same phase line, that is, the eddy arrives at Gizo ~20 days before it does at Misima. Therefore, we performed a simple analysis on subseasonal variability of satellite surface velocity from locations on the same phase line across the southern entrance (not shown). The resultant surface velocity also shows energetic subseasonal variation that is comparable to the surface velocity derived from ADT at the mooring locations. The extreme transport events in our observations are therefore actual fluctuations in the flow. In section 5.2.1, we will discuss the mechanism associated with these rapid fluctuations.

4.3.2. Seasonal Cycle

The seasonal cycle is computed from the observations by fitting annual and semiannual harmonics to the mooring/PIES transport time series. The seasonal cycle accounts for only 27% of the total variance reflecting a high variation from one year to another (Figure 6). The annual harmonic contributes 22%, while the semiannual harmonic contributes 5% to the total variance. The seasonal cycle has a maximum in July–August. The strengthening of the NGCC/NGCU results in broadening of the equatorward inflow that extends toward the eastern boundary of the Solomon Sea (Ganachaud et al., 2017; Germineaud et al., 2016); thus, the SPTW transported by the NGCC/NGCU is present in the eastern basin and high salinity at $\sigma_\theta = 24.5$ is observed at Gizo in July–August. A seasonal minimum inflow occurs in March–April when the Solomon Strait inflow brings anomalously fresh water into the Solomon Sea (Alberty, 2018) and at the Gizo site. The strong inflow from the Solomon Strait is mostly confined to the northern and eastern part of the basin (Melet, Gourdeau, & Verron, 2010) resulting in seasonally low saline water observed at Gizo in March–April; thus, distinct salinity seasonality is measured by the Gizo mooring (see section 4.1). The

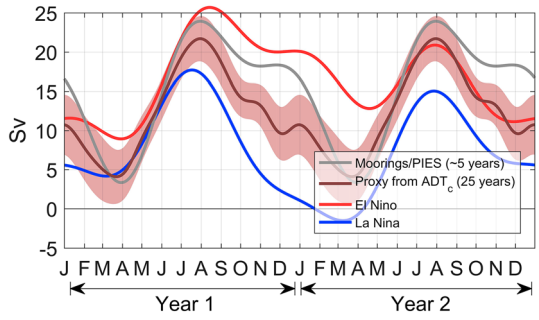

Figure 6. Seasonal cycle derived from fitting annual and semiannual harmonics to the mooring/Pressure with Inverted Echo Sounders (PIES) transport (black) and that derived from averaging proxy transport over 25 years (maroon) ±2 standard errors (shaded maroon). Semiannual, annual, and biennial harmonics of the volume transport over the developing phase (year 1) and decaying phase (year 2) of El Niño (red) and La Niña (blue) years are also presented.

seasonal cycle shows a rapid increase of the equatorward flow from April to July and a gradual decrease during the rest of the year particularly from October to December.

Since the proxy volume transport covers a much longer period of 25 years, the proxy seasonal cycle can be computed by averaging each day of the year of the proxy volume transport over 25 years (Figures 6 and 7a). Also in this case, the seasonal cycle of the proxy record has a minimum in March and maximum in July–August and explains 33% of the total variance. Similar to that derived from the observations, the proxy seasonal cycle shows asymmetry in the increasing and decreasing phases. The standard error ranges from 1 Sv in June–July to 1.9 Sv in March–April.

4.3.3. Interannual Variability

The proxy interannual transport, calculated by removing the seasonal cycle and variability faster than 400 days, ranges from −10.7 to 9.4 Sv and is highly correlated with the mean sea surface temperature in the Niño 3.4 region (Figure 7b). Niño 3.4 explains 66% of the variance of the proxy interannual transport with a mean lag of 2.7 months, although the lag varies across different ENSO events. The variable lag is likely due to changes in wind stress patterns in the interior of the Pacific Ocean during ENSO events that excite westward-propagating Rossby waves arriving at the western Pacific Ocean. During El Niño conditions, wind stress over the Solomon Island chain is northwestward and that over the equatorial Pacific is anomalously eastward causing negative wind stress curl between the equator and 15°S and east of the Solomon Island chain to approximately 140°W. Further south between 15°S and 25°S and west of 140°W, anomalous wind stress causes anomalous positive wind stress curl. The meridional opposing wind stress curl pattern in the western Pacific produces a meridional shoaling of the pycnocline toward the equator during El Niño. During La Niña conditions, the anomalous wind is generally in the opposite direction which causes deepening of the pycnocline toward the equator (Kessler & Cravatte, 2012). The mechanism suggests a modification of the SEC during both phases of ENSO events and implies that the dynamics governing the interannual variability of the downstream circulation into the Solomon Sea and the Coral Sea is fundamentally similar.

In addition, the semiannual, annual, and biennial harmonics were fitted to the proxy transport during El Niño (1997/1998, 2002/2003, 2009/2010, and 2015/2016) and La Niña years (1996/1997, 1999/2000, 2008/2009, and 2011/2012) to understand the impact of ENSO events on the seasonal cycle (Figure 6). The harmonics during El Niño conditions (September of the developing year [year 1] to April of the decaying year [year 2]) are significantly higher (5–13 Sv) compared to the 25-year proxy seasonal cycle. The seasonal minimum transport is anomalously high (at the end of March/beginning of April of year 2), and the period of seasonal maximum is prolonged (June of year 1 to January of year 2). This results in a weak seasonal cycle during El Niño years. The opposite conditions appear in the harmonics of the transport during La Niña years. Minimum transport is intensified (3–11 Sv lower than the proxy seasonal cycle) and extended from December of year 1 to April of year 2, while the maximum transport in July–August is significantly lower than the proxy seasonal cycle during both year 1 and year 2. Compared with a previously estimated proxy of transport anomalies from satellite-derived SLA between Papua New Guinea and Solomon Islands over the 1993 to mid-2004 period (Melet, Gourdeau, & Verron, 2010), our interannual proxy (Figure 7) generally has higher fluctuations due to a thicker depth layer of 500 m compared to their 150-m depth layer. While our proxy exhibits similar features, higher interannual volume transport is present at the beginning of 1993 and lower transport occurs at the beginning of 2003.

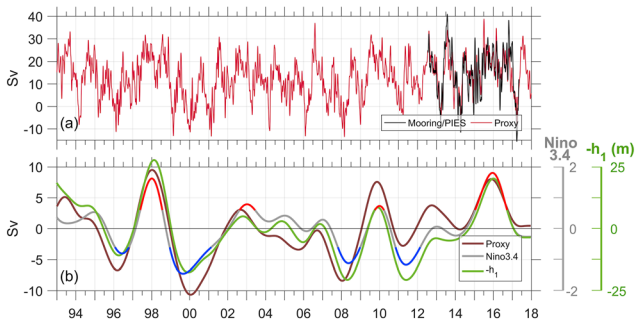

Figure 7. (a) The proxy volume transport (maroon) compared with the 10-day low-pass filtered mooring/Pressure with Inverted Echo Sounders (PIES) volume transport (black) over the upper 500 m of the water column, and (b) interannual component (>400 days) of the proxy volume transport (brown), interannual pycnocline depth near the Solomon Strait (h_1, green), and 2.7-month lag of Niño 3.4 index (gray). The Niño 3.4 index that is greater (less) than 0.6 (−0.6) is highlighted in red (blue) indicating El Niño (La Niña) condition.

4.3.4. The 2015/2016 El Niño

Both mooring/PIES observations and the proxy transport suggest that the interannual variability (>400 days) contributes 10% to the total variance.

The across-transect mean velocity profiles show a weakening of the seasonal poleward surface flow in January–May of 2015, during the onset of the 2015/2016 El Niño (Figure 3). The poleward flow is nearly absent during the El Niño in 2016. Also, the seasonal maximum subsurface NGCU core in July–August does not extend as deep in 2014–2016 compared to that in 2013, 2017, and 2018. To examine the impact of the 2015/2016 El Niño on the inflow seasonal variability, signals with frequencies higher than 60 days and lower than 400 days were filtered out from the volume transport in the surface, thermocline, and upper 500 m of the water column (Figures 8a and b). While the variability in the 60- to 400-day band is distinct prior to July 2014 and after September 2016, the filtered transport over the 0- to 500-m depth layer clearly shows a weakened seasonal signal in July 2014 to August 2016, which is contributed by both surface and thermocline layers. Thus, the observations suggest a weakening of both surface and thermocline seasonal cycles prior to the 2015/2016 El Niño event (second half of 2014) and a suppression during and after the El Niño (January 2015 to September 2016) similar to the finding from the proxy transport (Figure 6). Following the El Niño event in September–December 2016, the volume transport in the thermocline layer increases before it returns to the values observed during pre-El Niño conditions in 2017. The increase in volume transport following an El Niño event was similarly suggested by glider observations after the 2009 El Niño (Davis et al., 2012). The increase corresponds to a strong subsurface core that extends over 100- to 500-m depth comparable to that which usually occurs during the seasonal maximum in July–August (Figures 3 and 8a).

5. Forcing Mechanisms

5.1. Linear Rossby Wave Model

5.1.1. Model Description

As westward-propagating Rossby waves from the interior of the Pacific Ocean arrive at the Solomon Sea, they modify the pycnocline depth and affect the local circulation. Thus, following, for example, Chen and Qiu (2004) and Kessler and Gourdeau (2007), we adopted a 1.5-layer linear Rossby wave model that predicts the depth of pycnocline (h; positive downward) in the Solomon Sea based on wind stress curl in the interior of the Pacific Ocean. As the deeper layer is stagnant by assumption, the derived pycnocline depth only reflects the depth that is forced solely by wind stress curl in the interior:

$$\frac{\partial h}{\partial t} + c_r \frac{\partial h}{\partial x} + Rh = -\mathrm{curl}\left(\frac{\tau}{f\rho_0}\right), \tag{4}$$

where ρ_0 is surface density. Wind stresses (τ) are provided by the CCMP wind products and are averaged in 0.5° × 1° latitude-longitude grid boxes. The mean long Rossby wave speed (c_r) is calculated at each latitude (y) across the Pacific Ocean using values provided by Chelton et al. (1998). The damping timescale (R) is chosen to be 1/24 months^{-1} and the result is not sensitive to the choice of R. The assumption of a stagnant deeper layer (i.e., the NGCU) is clearly not valid, but the variability of the NGCU resembles that of the NGCC ($r = 0.73$). Therefore, the actual pycnocline depth slope still follows the sea surface slope but with a much smaller amplitude than that from the 1.5 layer case (the variability of the thermocline volume transport is ~5% bigger than that of the surface transport; Figure 5b). Thus, the presence of the NGCU in this scenario only modifies the *magnitude* of pycnocline depth difference (Δh) across the Solomon Sea, but the proportionality with the surface layer flow remains. At each latitude, the general solution can be found by integrating Ekman pumping (right-hand side of equation (4)) from the eastern boundary of the Pacific Ocean (x_E) along the Rossby wave characteristics:

$$h(x,y,t) = -\frac{1}{c_r(y)}\int_{x_E}^{x} \exp\left[-\frac{R}{c_r(y)}\left(x-x'\right)\right] \times \mathrm{curl}\left[\tau\left(x',y,t-\frac{x-x'}{c_r(y)}\right)/(f(y)\rho_0)\right]\mathrm{d}x' \tag{5}$$

Since wind stress and wind stress curl are much noisier than the volume transport particularly in the 3- to 10-day frequency band, the resultant h is much noisier compared to the volume transport. This reflects the limitation of the linear Rossby model in capturing variability of the inflow at high frequency. Therefore, a 10-day low-pass filter is applied to h and it is compared to the 10-day low-pass filtered volume inflow in the subsequent sections.

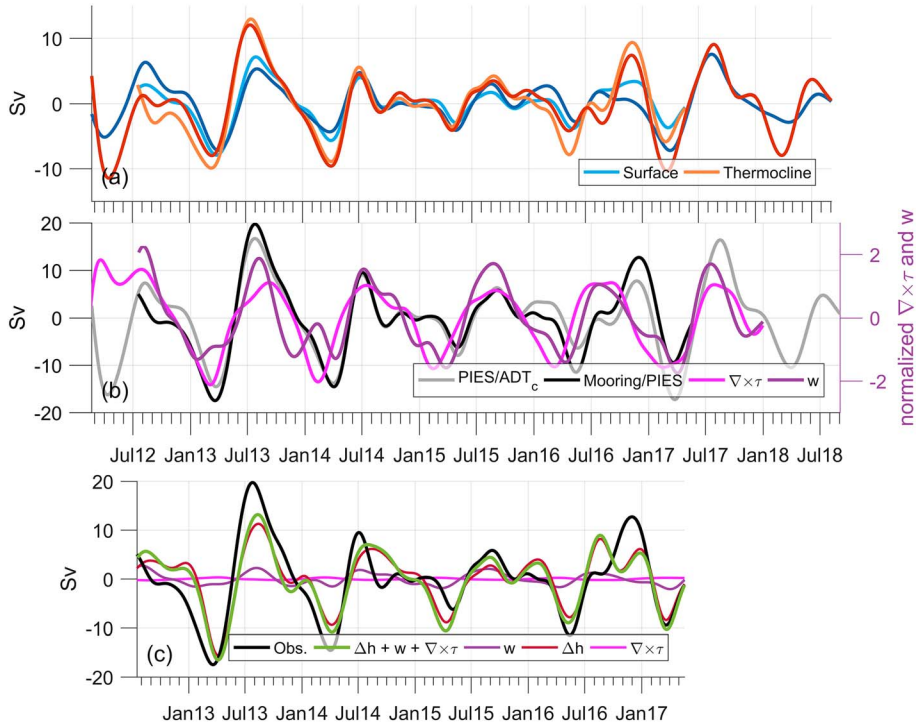

Figure 8. (a) The 60- to 400-day demeaned filtered volume transport in the surface (light blue) and thermocline (orange) layers estimated from the mooring/PIES observations and from the PIES/ADTc reconstruction (dark blue and red), (b) 60- to 400-day demeaned filtered total volume transport over the upper 500 m of the water column from mooring/PIES (black) and PIES/ADTc (gray) in sverdrups compared to 60- to 400-day filtered wind stress curl in the western subtropical Pacific ($\nabla \times \tau$, magenta) and filtered local Ekman pumping (w, purple) normalized by their standard deviation, (c) 60- to 400-day filtered volume transport from mooring/PIES observations (black) compared to modeled volume transport (green) estimated from multi-variable regression using filtered pycnocline depth difference (Δh), w, and $\nabla \times \tau$. The model transport is decomposed into transport (Sv) contributed by Δh (maroon), w (purple), and $\nabla \times \tau$ (magenta). PIES = Pressure with Inverted Echo Sounders; ADT = absolute dynamic topography.

5.1.2. The Observed Volume Transport

The locations where h is generated to produce Δh, the proxy for volume transport, were not at the actual mooring/PIES locations since the linear model only captures variability of h forced by Ekman pumping in the interior of the Pacific Ocean. The model also does not allow us to take the complex topography in the area into account and does not include the impact of coastal Kevin waves; the difference in h between the actual observing sites is therefore unlikely to adequately capture dynamics associated with the inflow. Rather, the locations were selected empirically based on the correlation between Δh and the NGCC and NGCU volume transports (Figure 9a). The difference between the pycnocline depth ($\Delta h = h_1 - h_2$) derived from the linear model evaluated at the Solomon Strait (h_1 at $x_1 = 156°$E, $y_1 = 6°$S) and the Gulf of Papua (h_2 at $x_2 = 144°$E, $y_2 = 14°$S; Figure 1) correlates well ($r = 0.81$) with the observed NGCC volume transport (Figure 9a). For the upper 500 m of the water column, Δh captures 46% of the total transport variance ($r = 0.68$). The decrease in the percentage of the explained variance indicates the reduced effect of the wind stress curl in the deeper part of the water column (~130–500 m). The pycnocline variation implies the influence of Rossby waves at all latitudes between 6° to 14°S that reach the Solomon Island chain and travel along the coastal waveguide within the NGCC. Positive correlation indicates shoaling of h_1 and deepening of h_2 corresponding to an equatorward NGCC and vice versa. Although some of the subseasonal variability including the extreme events in the NGCC is captured by Δh (e.g., in May–June 2013, June 2014, and January–February 2017), the model only explains a small fraction of the variance in the subseasonal frequency band.

5.1.3. The Proxy Volume Transport (Interannual Variability)

The linear Rossby wave model is also used to study the impact of Rossby waves on the interannual variability of the proxy inflow. The interannual component (>400 days) of h_1, h_2 and the proxy volume transport over

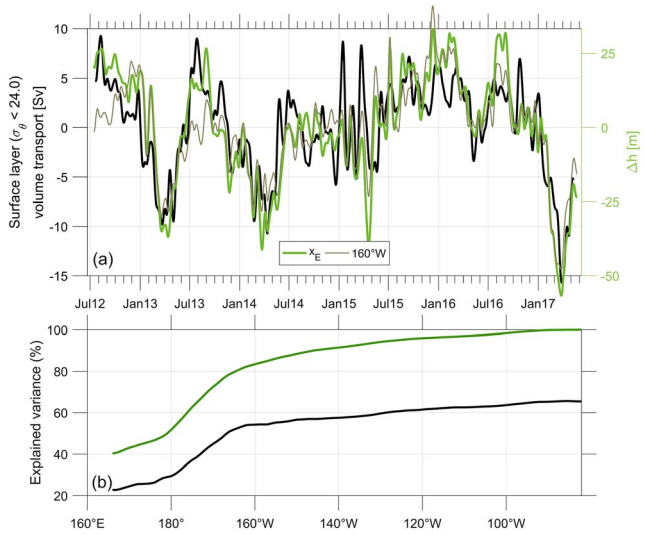

Figure 9. (a) 10-day low-pass filtered mooring/PIES surface volume transport with its mean removed (black) compared to Δh near the Solomon Strait (156°E, 6°S) and in the Gulf of Papua (144°E, 14°S) forced by wind stress curl to the west of the eastern boundary of the Pacific Ocean (x_E, bright green) and west of 160°W (thin dark green), and (b) percent of Δh (green) and the New Guinea Coastal Current (black) variance explained by Δh forced by wind stress curl to the west of each longitude.

1993–2017 period was examined. The interannual variability of both h_1 and h_2 are similar, despite a weaker signal and a lag in h_2 compared to h_1 due to its location further to the southwest and the slower propagation speed of Rossby waves there. The similarity is due to the interannual wind stress curl that is roughly uniform between the equator and 15°S to the west of 160°W (Kessler & Cravatte, 2012). Surprisingly, h_1 alone is a good indicator of the interannual variability of the Solomon Sea inflow over the upper 500 m of the water column (r = 0.93); it shoals during El Niño events and deepens during La Niña events (Figure 7b). This shows a strong association between Rossby waves arriving at the Solomon Strait and the Solomon Sea inflow over the top 500 m of the water column on the interannual timescales.

5.1.4. Contribution of Wind Stress Curl in the Pacific to Δh Variance

The cumulative variance of the pycnocline depth difference produced by the wind stress curl as a function of longitude (X) is calculated to understand the contribution of wind stress curl at each longitude (Qiu & Chen, 2010)

$$S(X)\equiv 1-\frac{\left\langle [\Delta h(x_E,t)-\Delta h(X,t)]^2\right\rangle}{\left\langle \Delta h^2(x_E,t)\right\rangle}, \tag{6}$$

where the angle bracket denotes the time average over the observational period (July 2012–August 2017) and $\Delta h(X,t)$ is the difference between $h_1(X,t)$ and $h_2(X,t)$ where $h_1(X,t)$ and $h_2(X,t)$ are computed similarly from integrating Ekman pumping from X to x_1 and x_2,

$$h_1(X,t) = -\frac{1}{c_r(y_1)}\int_X^{x_1} \exp\left[-\frac{R}{c_r(y_1)}(x_1-x')\right] \times \mathrm{curl}\left[\tau\left(x', y_1, t-\frac{x_1-x'}{c_r(y_1)}\right)/(f(y_1)\rho_0)\right]\mathrm{d}x' \tag{7}$$

Note that when replacing X with x_E, the result from equation (7) is the same as that from equation (5) when integrated to x_1 along y_1. The percentage of explained variance increases rapidly in the western Pacific Ocean, particularly to the west of 160°W (Figure 9b). The Δh forced by wind stress curl west of 160°W reproduces that forced by wind stress curl over the entire Pacific Ocean well and captures 54% of the total variance in the NGCC (Figure 9).

5.2. Local and Remote Winds

5.2.1. Subseasonal Timescale

Ekman pumping/suction ($w = \nabla\times\frac{\tau}{\rho f}$) and wind stress averaged in a 3° longitude × 1° latitude grid over and nearby the Solomon Sea are examined in an effort to understand the mechanism associated with the subseasonal variability and extreme transport events. The wind stress and wind stress curl are, however, much noisier than the volume transport particularly at frequencies higher than 10 days. Hence, a 10- to 60-day band-pass filter, which preserves characteristics of the extreme events reasonably well, is applied to the wind forcing and volume transport to examine the impact of wind stress and wind stress curl on the subsesasonal inflow.

Ekman pumping near Gizo (centered at 9.5°S, 159°E), where high variability in dynamic height is found, is reasonably correlated with the band-pass observations at a lead of 4–16 days; at a 11-day lead, it explains 24% of the variance and is significant at the 95% level (Figure 10a). Ekman suction is present at Gizo roughly 11 days before the maximum of the extreme events, while Ekman pumping is present about 11 days before the minimum of the events. A movie (not shown) of the band-pass Ekman pumping over the Solomon Sea finds that the extreme events are usually associated with changes in Ekman pumping at either side of the southern entrance. Prior to a sudden increase of the volume

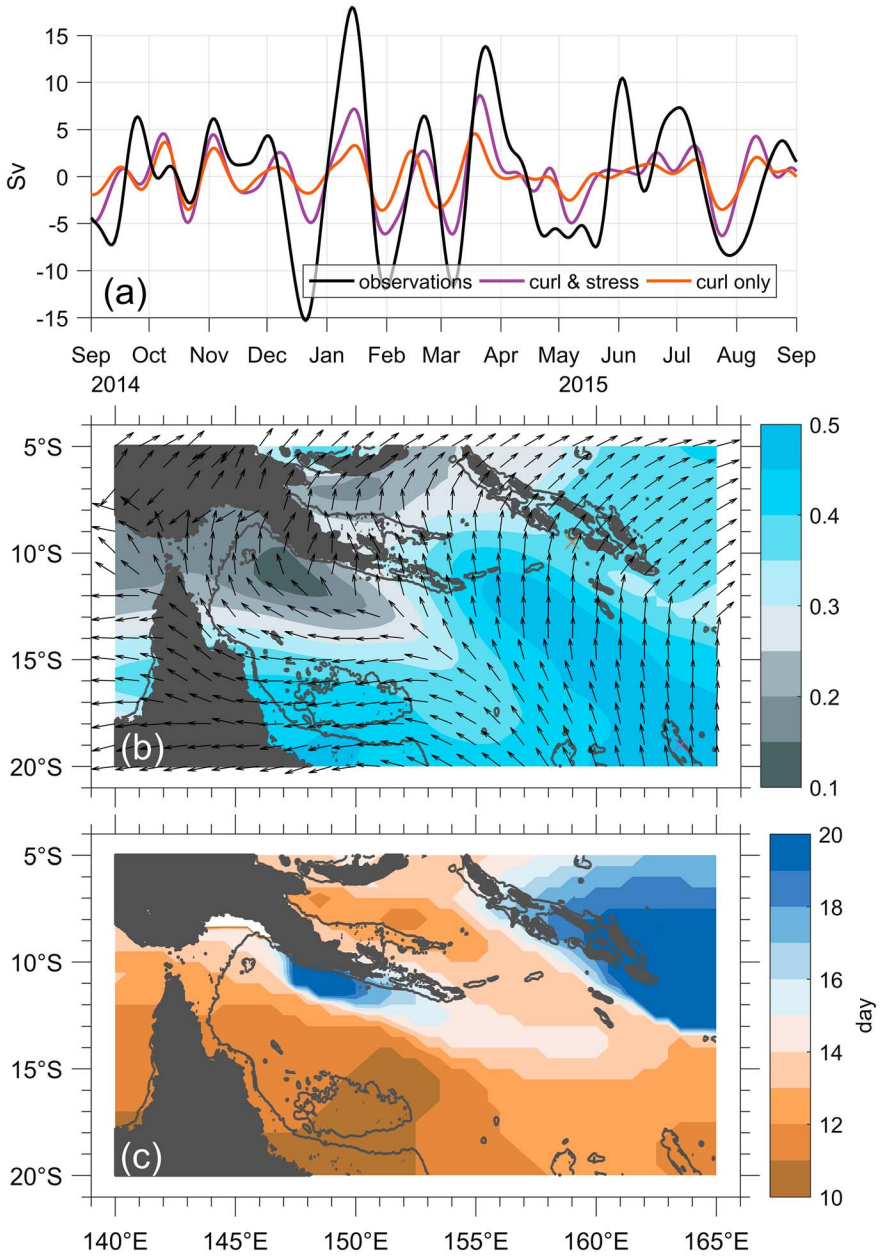

Figure 10. (a) Subseasonal (10–60 day) volume transport inflow (black) and estimated volume transport by linear regression with only wind stress curl that leads by 11 days (orange) and with both wind stress curl that leads by 11 days and concurrent wind stress (purple). (b) Direction of subseasonal wind stress (arrows) that yields maximum correlation between subseasonal volume transport and that calculated from the zonal and meridional wind stress through linear regression (color contour) with (c) the corresponding lead in the wind stress. The orange cross in (b) shows the location of wind stress curl used in the linear regression in (a), and the purple cross shows the location of maximum correlation between subseasonal volume transport and subseasonal wind stress.

transport, w increases at Gizo and decreases at Misima, which lowers the sea surface height at Gizo compared to that at Misima driving the flow toward the equator. The opposite is observed for a sudden volume transport decrease.

The effect of wind stress on the subseasonal inflow variation is examined by simultaneously regressing zonal and meridional subseasonal (10–60 day) wind stress against the subseasonal volume inflow varying the lag in the volume transport from 0 to 20 days. The coefficients in front of the zonal and meridional wind stress

components give the direction of wind stress that has the highest correlation to the subseasonal inflow (Peterson et al., 2012). High correlation values are found over the Coral Sea and south of the Solomon Sea when wind stress leads by 10–14 days (Figures 10b and 10c). Also, the inflow is mainly associated with southerly wind stress to the east of 155°E, south of 10°S. The highest correlation is found over the Coral Sea when wind stress leads by 11 days (19°S, 163.5°E; $r = 0.50$). The correlation decreases slightly with an increased lead in wind stress toward the southern entrance of the Solomon Sea implying that the subseasonal inflow variation is not locally driven by wind stress. Rather it suggests that the wind stress over the Coral Sea modifies the source of the NGCC/NGCU current system as the equatorward wind stress drives volume transport westward through Ekman dynamics creating a gradient in sea surface height that results in geostrophic equatorward volume transport. When considering the wind stress and Ekman pumping together through multivariable regression, the result explains 33% of the subseasonal variability over the observing period. However, over the period with pronounced extreme events (September 2014 to August 2015), the local and remote winds explain 58% of variance in the 10- to 60-day band (Figure 10a).

5.2.2. Variability Between 60 and 400 Days

The observed volume transport is first filtered to eliminate signals with frequencies higher than 60 days and lower than 400 days and is then compared to similarly filtered mean wind stress curl over the western subtropical Pacific and local Ekman pumping (Figure 8b). The annual variability of the circulation in the western subtropical Pacific is known to be driven by uniformly phased wind stress curl between 12° to 30°S as it alters the circulation of the subtropical gyre (Kessler & Gourdeau, 2007) and hence also potentially influences the Solomon Sea inflow. The mooring/PIES observations show an increase of the inflow with a lag of 34 days following an increase of wind stress curl averaged between 150° and 165°E, 10° and 20°S ($r = 0.71$). The time lag suggests a delayed response of the subtropical gyre circulation to the change in the wind stress curl. In addition, the effect of local Ekman pumping on the inflow is examined as it modifies annual variation of the surface velocity in the Solomon Sea (Melet, Gourdeau, Kessler, et al., 2010). Ekman pumping over the Solomon Sea exhibits clear variation; Ekman pumping (suction) is present in the western (eastern) part of the basin in August–September, while the opposite occurs in January–April. The Ekman pumping along either side of the basin correlates well with the inflow ($r = \sim 0.6$). However, a linear multivariable regression of the mean wind stress curl, local Ekman pumping, and Δh from the Rossby model against the observed inflow shows that 60- to 400-day variability of the inflow is mainly associated with Δh (Figure 8c); Δh alone explains 65% ($r = 0.81$) of the variability. An addition of the wind forcing insignificantly increases the explained variance to 66%. Although high correlations are found between the wind forcing and the volume inflow, they are due to their distinct seasonal cycle (Figure 8b). Also, both filtered local Ekman pumping and remote wind stress curl exhibit little interannual variation compared to the filtered transport, that is, seasonal cycle suppression in the Ekman pumping and wind stress curl is not apparent during the 2014–2016 period. Therefore, we conclude that the Rossby waves that propagated from the interior of the Pacific Ocean between 6° and 14°S mainly influences the 60–400 day variability of the 0- to 500-m inflow at the southern entrance of the Solomon Sea.

6. Discussion

6.1. Extreme Subseasonal Changes in the Volume Inflow

The extreme transport events measured by the moorings and PIES are as large as the seasonal fluctuation of the inflow (Figure 5). The events are unlikely to be associated with mesoscale activities in this region (Figure 5b; Appendix B). They are more abundant and prevalent during the 2015/2016 El Niño (Figure 5c). During the neutral ENSO conditions (prior to July 2014 and after September 2016), the increasing (decreasing) extreme events are larger and more abundant between March and July of 2013 and 2014 (between August and February of 2012/2013, 2013/2014, and 2016/2017; Figure 5a). This suggests a connection between the extreme events and the seasonal cycle; sudden increases (decreases) in the volume transport are more dominant during the increasing (decreasing) phase of the seasonal cycle. The local wind stress curl produces a pycnocline tilt along the transect resulting in a sudden increase or decrease of the volume transport in the top 500 m of the water column, while the remote wind stress over the Coral Sea (19°S, 163.5°E) potentially modifies the source of the NGCC/NGCU current system. Overall, the local and remote winds together only explain 33% of the subseasonal variance (Figure 10) leaving a large portion of the variance unexplained. Intraseasonal Kelvin waves driven by anomalous westerly winds, such as those

created by the Madden Julian Oscillation (MJO), could play an important role in influencing the observed subseasonal transport; intraseasonal Kelvin waves become more energetic and the MJO extends further east during El Niño conditions (Kessler, 2001; Rydbeck et al., 2019). However, examining the influence of intraseasonal Kelvin waves on the subseasonal variability of the Solomon Sea inflow is beyond the scope of this study.

6.2. Sixty- to Four Hundred-Day Variability and the Seasonal Cycle

Variability between 60 and 400 days accounts for half of the total variance in the volume transport at the southern entrance of the Solomon Sea; the variability is dominated by the seasonal cycle (annual plus semi-annual harmonics) that accounts for 27% of the total variance (Figure 6). While previous studies suggest the influence of western Pacific subtropical wind stress curl, local Ekman pumping, and westward propagating Rossby waves on Solomon Sea circulation, we found that only the impact of Rossby waves forced by Ekman pumping in the interior of the Pacific (equation (4)) significantly influences the 60- to 400-day transport variability (Figure 8c). The Rossby waves potentially determine the seasonal latitudinal shift of the SEC that previous observations and numerical studies have identified to influence the circulation in the Solomon Sea (Chen & Qiu, 2004; Cravatte et al., 2011; Melet, Gourdeau, Kessler, et al., 2010). The SEC core located at 8°–10°S strengthens the westward-flowing NVJ and increases the volume transport into the southern Solomon Sea during the period of maximum inflow (July–August), whereas the SEC core is near the Solomon Strait (3°–6°S) during the period of minimum inflow at the southern entrance (March–April). The northward migration of the SEC during March–April strengthens the flow into the Solomon Sea at the Solomon Strait (Alberty, 2018; Germineaud et al., 2016). At the surface, the Solomon Strait inflow turns southeastward and exits the Solomon Sea at the southern entrance (Hristova & Kessler, 2012) consistent with the seasonal poleward surface flow from the mooring/PIES observations (Figure 3).

6.3. The 2015/2016 El Niño Compared With Other El Niño Events

The intensity and development of the 2015/2016 El Niño was very different from other El Niño events (Jacox et al., 2016; McPhaden, 2015). The 2015/2016 El Niño developed, while the equatorial Pacific was already anomalously warm due to anomalous bursts of westerly winds along the equator in the previous year (at the beginning of 2014). This results in one of only a few El Niño events that are associated with warming of the tropical Pacific extending over a 1-year period (Harrison & Larkin, 1996; Levine & McPhaden, 2016; McPhaden, 2015). During the period when the tropical warm water volume grows quickly in the first half of 2014 (Levine & McPhaden, 2016), the NGCC/NGCU shows no significant change. However, seasonality in both the NGCC and NGCU is suppressed in late 2014 (Figure 3, 5, and 8) when the El Niño development ceased due to a strengthening of the easterlies (Levine & McPhaden, 2016), that is, the suppression occurs even before the mature phase of the 2015/2016 El Niño in the second half of 2015. Although the warm condition ends roughly in June 2016 (Figure 7b), the seasonal cycle remains suppressed until August 2016. This suggests a strong response of the LLWBC during the 2015/2016 event to the tropical warm water volume with a lag of about 3–6 months. During more "typical" El Niño events, the inflow interannual variability is expected to not exceed 9 Sv (Figure 7b) and the seasonal cycle should not be suppressed for a period longer than 2 years.

7. Summary

The mooring and PIES measurements, together with the remotely sensed satellite altimetry, provide the first high temporal resolution volume inflow observations at the southern entrance of the Solomon Sea (Figure 5) along with the mean across-transect velocity profiles in the upper 500 m of the water column (Figure 3). Velocity profiles are also reconstructed from the satellite surface velocity and PIES subsurface velocity as a linear combination of the leading vertical EOF modes derived from the mooring/PIES measurements. The strong subsurface flow in July–August is correctly estimated by the reconstruction, and the surface poleward flow during January–May period is clearly observed. The reconstructed velocity partially resolves the high-frequency variability that is not observed in the satellite surface velocity alone. Both time series reveal energetic volume fluctuation at subseasonal, seasonal, and interannual timescales.

The majority of the energy in the total variance lies within the 60- to 400-day frequency band; the dominant variability is described by weak equatorward volume transport in January–May and strong equatorward

transport in June–October consistent with that described by previous studies (Cravatte et al., 2011; Davis et al., 2012; Kessler et al., 2019; Figures 6 and 8b). The weak flow is due to the seasonal reversal of the NGCC, while the strong flow is caused by seasonal strengthening of the NGCU (Figures 3 and 5). The observations show that the inflow is primarily driven by westward-propagating Rossby waves at the seasonal timescale consistent with findings from previous numerical and altimetric studies (Chen & Qiu, 2004; Gourdeau et al., 2014; Melet, Gourdeau, Kessler, et al., 2010; Melet, Gourdeau, & Verron, 2010). The Δh derived from the linear Rossby model (equation (4)), particularly between 6° and 14°S, west of 160°W, can reproduce 54% of the inflow variance (Figure 9).

The interannual variability of the inflow is closely related to ENSO as described by earlier observational studies (Davis et al., 2012; Zilberman et al., 2013; Kessler et al., 2019; Figure 7b). In addition, our observations show the strengthening of the equatorward flow in the upper 500 m of the water column accompanied by the weakening of the seasonal cycle (Figure 5); the El Niño suppresses the seasonal cycles of both the NGCC and the NGCU (Figures 3 and 8). The proxy transport shows the weakening of seasonal cycle during other El Niño events, particularly from September of year 1 to April of year 2 (Figure 6). During La Niña conditions, the phase of seasonal minimum flow is prolonged and the minimum is intensified. The inflow fluctuation is also well captured by the modeled pycnocline depth near the Solomon Strait; it explains 86% of the interannual variance (Figure 7b).

In addition, the high temporal resolution of the observations allows us to examine the inflow variability that is as fast as 3–60 days that accounts for 37% of the total variance. Vigorous subseasonal volume fluctuations that contain more than a third of the total energy in the volume transport are found (Figures 5c and 5d) emphasizing the need for continuous high temporal resolution inflow monitoring. The subseasonal fluctuation can be explained partly by the local and remote winds (Figure 10). Still a large fraction of the subseasonal variability cannot be explained and remains an open question for future studies.

Appendix A: Numerical model

A global strongly eddy active Ocean General Circulation Model, the 0.1° Parallel Ocean Program coupled to the Los Alamos Sea Ice Model (POP/CICE) run in the Community Earth System Model framework (McClean et al., 2018), was used to estimate uncertainty associated with volume transport derived from mooring/PIES measurements. POP is a three-dimensional, z level, primitive equation model (Dukowicz & Smith, 1994). It was configured on a global tripole grid with 42 vertical levels and partial bottom cells. It is forced with Co-ordinated Ocean-ice Reference Experiments II interannually varying atmospheric surface fluxes (Large & Yeager, 2009) and run from 1948 to 2009. POP's horizontal resolution corresponds to approximately 11 km in the Solomon Sea. The POP output analyzed here consists of three-dimensional daily averaged velocity and density fields for 2005–2009.

Appendix B: Estimating Error in Volume Transport Calculation due to Eddies

Assuming a constant f and no cross-passage structure along the entire transect between the two end point moorings can result in an error in our volume transport calculation, particularly during times when eddies propagate across the transect. Therefore, we estimated uncertainty in our calculation arising from across-transect eddy propagation as an artifact of these assumptions. We identified eddies manually from a satellite SLA field as a closed SLA contour with a minimum or maximum vertical displacement exceeding 10 cm. For each eddy, the uncertainty (V_e, shown in Figure 5b) was estimated as the difference between that representing the mooring (V_{moor}) and the "more resolved" volume transport (V_{res}). Only the end point SLA and a constant f ($f_{\mathrm{mid}} = f$ at 9.4°S) were used to calculate V_{moor}, while all available SLA along the transect binned into 0.12° bin (corresponding to ~0.06° latitude) and f parameter at the center of each bin (f_i) were used to compute V_{res}. Both V_{moor} and V_{res} were estimated at each daily time step (t):

$$V_{\mathrm{moor}}(t) = \frac{gD}{f_{\mathrm{mid}}}\left(\eta_{n+1}(t) - \eta_1(t)\right), \tag{A1}$$

$$V_{\mathrm{res}}(t) = \sum_{i=1}^{n} \frac{gD}{f_i}\Delta\eta_i(t), \tag{A2}$$

$$V_e(t) = V_{\mathrm{moor}}(t) - V_{\mathrm{res}}(t). \tag{A3}$$

where D is a constant depth layer of 500 m, $\eta_i(t)$ is SLA at the western side of bin i at time step t, n represents the number of bins along the transect (equal to 40), and $\Delta\eta_i$ tern side of bin i ($\Delta\eta_i = \eta_{i+1} - \eta_i$).

Acknowledgments
This project is a part of the Consortium on the Ocean's Role in Climate (CORC) supported by National Oceanic and Atmospheric Administration (NOAA) through grants NOAA NA15OAR4320071. This material is based upon work supported by the National Aeronautics and Space Administration under grant 80NSSC17K0373 to Arachaporn Anutaliya. Any opinions, findings, and conclusions or recommendations expressed in this material are those of the author(s) and do not necessarily reflect the views of the National Aeronautics and Space Administration. Janet Sprintall was supported by National Science Foundation grant OCE1029487. Julie L. McClean was supported by DOE U.S. Office of Science Award DE-SC0012778. Mooring and PIES measurements were collected and made freely available by the international OceanSITES project and the national programs that contribute to it. The authors would like to thank R. Davis from Scripps Institution of Oceanography (SIO) and W. Kessler (NOAA/Pacific Marine Environmental Laboratory) for the Spray underwater glider measurements (under the CORC program) and your generous help regarding the data handling. Argo data were collected and made freely available by the International Argo Program and the national programs that contribute to it (http://www.argo.ucsd.edu and http://argo.jcommops.org). The Argo Program is part of the Global Ocean Observing System. This study has been conducted using E.U. Copernicus Marine Service Information (http://marine.copernicus.eu/services-portfolio/access-to-products/?option=com_csw&view=details&product_id=SEALEVEL_GLO_PHY_L4_REP_OBSERVATIONS_008_047). CCMP Version-2.0 vector wind analyses are produced by Remote Sensing Systems. Data are available at www.remss.com. We would like to acknowledge high-performance computing support from Yellowstone (ark:/85065/d7wd3xhc) provided by NCAR's Climate Simulation Laboratory, sponsored by the National Science Foundation. Funding for the POP simulation was provided by a DOE BER grant entitled "Ultra High Resolution Global Climate Simulation" via a Los Alamos National Laboratory subcontract. We are grateful for support by the local authorities and partners, including Chalapan Kaluwin of the University of Papua New Guinea, cognizant PNG agency, Danny Kennedy of Dive Gizo, and Chanel Iroi of the Solomon Islands Meteorological Service. Thanks to Bruce Cornuelle,

References

Alberty, M. S. (2018). Water mass transport and transformation in the tropics and Arctic, (Doctoral dissertation). Retrieved from eScholarship. (https://escholarship.org/uc/item/9rf158pq). San Diego, CA: University of California San Deigo.

Chelton, D. B., de Szoeke, R. A., Schlax, M. G., El Naggar, K., & Siwertz, N. (1998). Geographical variability of the first-baroclinic Rossby radius of deformation. *Journal of Physical Oceanography*, *28*, 433–460.

Chen, S., & Qiu, B. (2004). Seasonal variability of the South Equatorial Countercurrent. *Journal of Geophysical Research*, *109*, C08003. https://doi.org/10.1029/2003JC002243

Codiga, D. L. (2011). Unified tidal analysis and prediction using the UTide Matlab functions (Technical Report 2011-01). Graduate School of Oceanography, University of Rhode Island, Narragansett, RI. ftp://www.po.gso.uri.edu/pub/downloads/codiga/pubs/2011Codiga-UTide-Report.pdf

Cravatte, S., Ganachaud, A., Duong, Q.-P., Kessler, W. S., Eldin, G., & Dutrieux, P. (2011). Observed circulation in the Solomon Sea from SADCP. *Progress in Oceanography*, *88*(1-4), 116–130. https://doi.org/10.1016/j.pocean.2010.12.015

Davis, S. E., Kessler, W. S., & Sherman, J. T. (2012). Gliders measure western boundary current transport from the South Pacific to the equator. *Journal of Physical Oceanography*, *42*(11), 2001–2013. https://doi.org/10.1175/JPO-D-12-022.1

Djath, B., Verron, J., Melet, A., Gourdeau, L., Barnier, B., & Molines, J.-M. (2014). Multiscale dynamical analysis of a high-resolution numerical model simulation of the Solomon Sea Circulation. *Journal of Geophysical Research: Oceans*, *119*, 6286–6304. https://doi.org/10.1002/2013JC009695

Dukowicz, J. K., & Smith, R. D. (1994). Implicit free-surface method for the Bryan-Cox-Semtner ocean model. *Journal of Geophysical Research*, *99*(C4), 7991–8014. https://doi.org/10.1029/93JC03455

Fine, R. A., Lukas, R., Bingham, F. M., Warner, M. J., & Gammon, R. H. (1994). The western equatorial pacific: A water mass crossroads. *Journal of Geophysical Research*, *99*(C12), 25,063–25,080. https://doi.org/10.1029/94JC02277

Ganachaud, A., Cravatte, S., Melet, A., Schiller, A., Holbrook, N. J., Sloyan, B. M., et al. (2014). The Southwest Pacific Ocean circulation and climate experiment (SPICE). *Journal of Geophysical Research: Oceans*, *119*, 7660–7686. https://doi.org/10.1002/2013JC009678

Ganachaud, A., Cravatte, S., Sprintall, J., Germineaud, C., Alberty, M., Jeandel, C., et al. (2017). The Solomon Sea: Its circulation, chemistry, geochemistry and biology explored during two oceanographic cruises. *Elementa: Science of the Anthropocene*, *5*(0), 33. https://doi.org/10.1525/elementa.221

Gasparin, F., Ganachaud, A., Maes, C., Marin, F., & Eldin, G. (2012). Oceanic transports through the Solomon Sea: The bend of the New Guinea Coastal Undercurrent. *Geophysical Research Letters*, *39*, L15608. https://doi.org/10.1029/2012GL052575

Germineaud, C., Ganachaud, A., Sprintall, J., Cravatte, S., Eldin, G., Alberty, M., & Privat, E. (2016). Pathways and water properties of the thermocline and intermediate water in the Solomon Sea. *Journal of Physical Oceanography*, *46*(10), 3031–3049. https://doi.org/10.1175/JPO-D-16-0107.1

Gourdeau, L., Verron, J., Chaigneau, A., Cravatte, S., & Kessler, W. (2017). Complementary Use of glider data, altimetry, and model for exploring mesoscale eddies in the tropical Pacific Solomon Sea. *Journal of Geophysical Research: Oceans*, *122*, 9209–9229. https://doi.org/10.1002/2017JC013116

Gourdeau, L., Verron, J., Melet, A., Kessler, W., Marin, F., & Djath, B. (2014). Exploring the mesoscale activity in the Solomon Sea: A complementary approach with a numerical model and altimetric data. *Journal of Geophysical Research: Oceans*, *119*, 2290–2311. https://doi.org/10.1002/2013JC009614

Grenier, M., Cravatte, S., Blanke, B., Menkes, C., Koch-Larrouy, A., Durand, R., et al. (2011). From the western boundary currents to the pacific equatorial undercurrent: Modeled pathways and water mass evolutions. *Journal of Geophysical Research*, *116*, C12044. https://doi.org/10.1029/2011JC007477

Gu, D. F., & Philander, S. G. H. (1997). Interdecadal climate fluctuations that depend on exchanges between the tropics and extratropics. *Science*, *275*(5301), 805–807. https://doi.org/10.1126/science.275.5301.805

Harrison, D. E., & Larkin, N. K. (1996). The COADS sea level pressure signal: A near-global El Niño composite and time series view, 1946-1993. *Journal of Climate*, *9*(12), 3025–3055. https://doi.org/10.1175/1520-0442(1996)009<3025:TCSLPS>2.0.CO;2

Holgate, S. J., Matthews, A., Woodworth, P. L., Rickards, L. J., Tamisiea, M. E., Bradshaw, E., et al. (2013). New data systems and products at the permanent service for mean sea level. *Journal of Coastal Research*, *29*(3), 493–504. https://doi.org/10.2112/JCOASTRES-D-12-00175.1

Hristova, G. H., & Kessler, W. S. (2012). Surface circulation in the Solomon Sea derived from Lagrangian drifter observations. *Journal of Physical Oceanography*, *42*(3), 448–458. https://doi.org/10.1175/JPO-D-11-099.1

Hristova, G. H., Kessler, W. S., McWilliams, J. C., & Molemaker, M. J. (2014). Mesoscale variability and its seasonality in the Solomon and Coral Seas. *Journal of Geophysical Research: Oceans*, *119*, 4669–4687. https://doi.org/10.1002/2013JC009741

Jacox, M. G., Hazen, E. L., Zaba, K. D., Rudnick, D. L., Edwards, C. A., Moore, A. M., & Bograd, S. J. (2016). Impacts of the 2015–2016 El Niño on the California Current System: Early assessment and comparison to past events. *Geophysical Research Letters*, *43*, 7072–7080. https://doi.org/10.1002/2016GL069716

Kanzow, T., Send, U., Zenk, W., Chave, A. D., & Rhein, M. (2006). Monitoring the integrated deep meridional flow in the tropical North Atlantic: Long-term performance of a geostrophic array. *Deep-Sea Res. I*, *53*(3), 528–546. https://doi.org/10.1016/j.dsr.2005.12.007

Kennelly, M., Tracy, K., & Watts, D. R. (2007). Inverted Echo Sounder data processing manual. University of Rhode Island Graduate School of Oceanography Tech. Rep. 2007-02. [Available online at http://digitalcommons.uri.edu/physical_oceanography_techpts/2/.]

Kessler, W. S. (2001). EOF representations of the Madden-Julian Oscillation and its connection with ENSO. *Journal of Climate*, *14*(13), 3055–3061. https://doi.org/10.1175/1520-0442(2001)014<3055:EROTMJ>2.0.CO;2

Kessler, W. S., & Cravatte, S. (2012). ENSO and short-term variability of the South Equatorial Current entering the Coral Sea. *Journal of Physical Oceanography*, *43*(5), 956–969. https://doi.org/10.1175/JPO-D-12-0113.1

Kessler, W. S., & Gourdeau, L. (2007). The annual cycle of circulation of the southwest subtropical Pacific, Analyzed in an ocean GCM. *Journal of Physical Oceanography*, *37*(6), 1610–1627. https://doi.org/10.1175/JPO3046.1

Sarah Gille, Shantong Sun, and Marion Alberty (all SIO) for helpful discussion and help improve the results. Thanks to three anonymous reviewers for their constructive comments.

Kessler, W. S., Hristova, H. G., & Davis, R. E. (2019). Equatorward western boundary transport from the South Pacific: Glider observations, dynamics and consequences. *Progress in Oceanography*, *175*, 208–225. https://doi.org/10.1016/j.pocean.2019.04.005

Large, W. G., & Yeager, S. G. (2009). The global climatology of an interannually varying air–sea flux data set. *Climate Dynamics*, *33*(2-3), 341–364. https://doi.org/10.1007/s00382-008-0441-3

Levine, A. F. Z., & McPhaden, M. J. (2016). How the July 2014 easterly wind burst gave the 2015–2016 El Niño a head start. *Geophysical Research Letters*, *43*, 6503–6510. https://doi.org/10.1002/2016GL069204

McClean, J. L., Bader, D. C., Maltrud, M. E., Evans, K. J., Taylor, M. A., Tang, Q., et al. (2018). High-resolution fully-coupled ACME v0.1 approximate present day transient simulations. Abstract OM44C-2143, presented at the Ocean Sciences Meeting, Portland, OR, 12-16 Feb.

McCreary, J. P., & Lu, P. (1994). Interaction between the subtropical and equatorial ocean circulations: The subtropical cell. *Journal of Physical Oceanography*, *24*(2), 466–497. https://doi.org/10.1175/1520-0485

McPhaden, M. J. (2015). Playing hide and seek with El Niño. *Nature Climate Change*, *5*(9), 791–795. https://doi.org/10.1038/nclimate2775

McPhaden, M. J., & Zhang, D. X. (2002). Slowdown of the meridional overturning circulation in the upper Pacific Ocean. *Nature*, *415*(6872), 603–608. https://doi.org/10.1038/415603a

Melet, A., Gourdeau, L., Kessler, W., Verron, J., & Molines, J. (2010). Thermocline circulation in the Solomon Sea: A modeling study. *Journal of Physical Oceanography*, *31*, 13324–11345.

Melet, A., Gourdeau, L., & Verron, J. (2010). Variability in Solomon Sea circulation derived from altimeter sea level data. *Ocean Dynamics*, *60*(4), 883–900. https://doi.org/10.1007/s10236-010-0302-6

Melet, A., Gourdeau, L., Verron, J., & Djath, B. (2013). Solomon sea circulation and water mass modifications: Response at ENSO time-scales. *Ocean Dynamics*, *63*(1), 1–19. https://doi.org/10.1007/s10236-012-0582-0

Permanent Service for Mean Sea Level (PSMSL), 2019, "Tide gauge data", Retrieved 20 May 2019 from http://www.psmsl.org/data/obtaining/.

Peterson, I., Hamilton, J., Prinsenberg, S., & Pettipas, R. (2012). Wind-forcing of volume transport through Lancaster Sound. *Journal of Geophysical Research*, *117*, C11018. https://doi.org/10.1029/2012JC008140

Picaut, J., Ioualalen, M., Menkes, C., Delcroix, T., & McPhaden, M. J. (1996). Mechanism of the zonal displacements of the Pacific Warm Pool: Implications for ENSO. *Science*, *274*(5292), 1486–1489. https://doi.org/10.1126/science.274.5292.1486

Qiu, B., & Chen, S. (2004). Seasonal modulations in the eddy field of the South Pacific Ocean. *Journal of Physical Oceanography*, *34*(7), 1515–1527. https://doi.org/10.1175/1520-0485(2004)034<1515:SMITEF>2.0.CO;2

Qiu, B., & Chen, S. (2010). Interannual-to-decadal variability in the bifurcation of the North Equatorial Current off the Philippines. *Journal of Physical Oceanography*, *40*(11), 2525–2538. https://doi.org/10.1175/2010JPO4462.1

Rio, M. H., & Hernandez, F. (2004). A mean dynamic topography computed over the world ocean from altimetry, in situ measurements, and a geoid model. *Journal of Geophysical Research*, *109*, C12032. https://doi.org/10.1029/2003JC002226

Rydbeck, A. V., Jensen, T. G., & Flatau, M. (2019). Characterization of intraseasonal Kelvin waves in the equatorial Pacific Ocean. *Journal of Geophysical Research: Oceans*, *124*(3), 2028–2053. https://doi.org/10.1029/2018JC014838

Thomson, R. E., & Emery, W. J. (2014). *Data analysis methods in physical oceanography*. Waltham, MA: Elsevier Science. Retrieved from. http://roger.ucsd.edu/record=b8259868~S9

Tsuchiya, M., Lukas, R., Fine, R. A., Firing, E., & Lindstrom, E. (1989). Source waters of the Pacific Equatorial Undercurrent. *Progress in Oceanography*, *23*(2), 101–147. https://doi.org/10.1016/0079-6611(89)90012-8

Wang, B., Wu, R., & Lukas, R. (2000). Annual adjustment of the thermocline in the tropical Pacific Ocean. *Journal of Climate*, *13*(3), 596–616. https://doi.org/10.1175/1520-0442(2000)013<0596:AAOTTI>2.0.CO;2

Waworuntu, J. M., Fine, R. A., Olson, D. B., & Gordon, A. L. (2000). Recipe for Banda Sea water. *Journal of Marine Research*, *58*(4), 547–569. https://doi.org/10.1357/002224000321511016

Wentz, F. J., Scott, J., Hoffman, R., Leidner, M., Atlas, R., & Ardizzone, J. (2015). Remote Sensing Systems Cross-Calibrated Multi-Platform (CCMP) 6-hourly ocean vector wind analysis product on 0.25 deg grid, Version 2.0, 2012-2017. Remote sensing systems, Santa Rosa, CA. Available online at www.remss.com/measurements/ccmp. Accessed 23 Mar 2018.

Zilberman, N. V., Roemmich, D. H., & Gille, S. T. (2013). The mean and the time variability of the shallow meridional overturning circulation in the tropical South Pacific Ocean. *Journal of Climate*, *26*(12), 4069–4087. https://doi.org/10.1175/JCLI-D-12-00120.1